Available online at www.sciencedirect.com
ScienceDirect
Journal of Solid State Chemistry 180 (2007) 1698–1707
JOURNAL OF SOLID STATE CHEMISTRY
www.elsevier.com/locate/jssc

Crystal structures, charge and oxygen-vacancy ordering in oxygen deficient perovskites $SrMnO_x$ ($x<2.7$)

Leopoldo Suescun[a,b,*,1], Omar Chmaissem[a,b], James Mais[b], Bogdan Dabrowski[a,b], James D. Jorgensen[a,†]

[a]*Materials Science Division, Argonne National Laboratory, Argonne, IL 60439, USA*
[b]*Physics Department, Northern Illinois University, DeKalb, IL 60115, USA*

Received 9 January 2007; received in revised form 14 March 2007; accepted 24 March 2007
Available online 28 March 2007

Abstract

Bulk $SrMnO_x$ samples with oxygen contents $2.5 \leqslant x < 2.7$ have been studied using a combination of neutron time-of-flight and high-energy high-resolution synchrotron X-ray diffraction measurements along with thermogravimetric analysis. We report the identification and characterization of two new oxygen-vacancy ordered phases, $Sr_5Mn_5O_{13}$ ($SrMnO_{2.6}$-tetragonal $P4/m$ $a = 8.6127(3)$ Å, $c = 3.8102(2)$ Å) and $Sr_7Mn_7O_{19}$ ($SrMnO_{2.714}$-monoclinic $P2/m$ $a = 8.6076(4)$ Å, $b = 12.1284(4)$ Å, $c = 3.8076(2)$ Å, $\gamma = 98.203(2)^\circ$). The nuclear and magnetic structures of $Sr_2Mn_2O_5$ are also reported ($SrMnO_{2.5}$ nuclear: orthorhombic *Pbam*, magnetic: Orthorhombic *Ay* type P_cbam with $c_M = 2c$). In the three phases, oxygen-vacancies are ordered in lines running along one of the (100) directions of the parent cubic perovskite system. Oxygen-vacancy ordering allows the charge and orbital ordering of the Mn^{3+} and Mn^{4+} cations in the new phases.

Keywords: Manganites; Structure determination; Oxygen vacancy-ordering; Synchrotron X-ray powder diffraction; Neutron time-of-flight powder diffraction

1. Introduction

Perovskites of the general formula ABO_x have been extensively studied for the last three decades due to their display of a plethora of physical properties with technological interest that depend on the processing conditions, oxygen content and ordering. In particular, members of the $SrMnO_x$ system have been known to crystallize in different thermodynamically and kinetically stable structures depending on the precise preparation conditions (temperature, heating/cooling rate, oxygen partial pressure, isostatic pressure, etc.) and convert to the stable ones upon further processing [1]. Up to this date, several phases have been identified for $2.5 < x < 3$ [1–4]. Among these, oxygen deficient and vacancy disordered perovskite phases with x close to 3 have been shown to display mixed electronic and ionic conductivity [2]. However, the low stability of the perovskite $SrMnO_x$ phases at temperatures above 700 °C and their transformation into hexagonal α-$SrMnO_{3-\delta}$ [1,2] has prevented their use in actual devices.

The lowest disordered oxygen content was reported in $SrMnO_{2.66}$ displaying the $GdFeO_3$ structure type [2] however no detailed structural data has been provided for this phase. To date, $Sr_2Mn_2O_5$ (nominally $SrMnO_{2.5}$) is the only definitely oxygen-ordered phase identified in the $SrMnO_x$ system. This phase was initially described in a brownmillerite-type structure [3,4] but subsequent reports [5–7] have shown convincing evidence that $Sr_2Mn_2O_5$ is isostructural with $Ca_2Mn_2O_5$ [8] in which the Mn^{3+} cations occupy square pyramidal sites that can be best

*Corresponding author. Argonne National Laboratory, Materials Science Division, Bldg 223, 9700 S. Cass Ave, Argonne, IL 60439, USA. Fax: +1 30 252 7777.
E-mail address: leopoldo@anl.gov (L. Suescun).
[1]Permanent Address: Cryssmat-Lab/Cátedra de Física/DETEMA Facultad de Química, Universidad de la República P.O. Box 1157, Montevideo, Uruguay.
[†]Deceased.

0022-4596/$ - see front matter © 2007 Elsevier Inc. All rights reserved.
doi:10.1016/j.jssc.2007.03.020

described using the orthorhombic *Pbam* symmetry. In this structure, the *A* or *B* sites are unique and four oxygen sites are available with one of them being vacant. Oxygen vacancies order along the primitive [100] perovskite axis forming pseudo-hexagonal channels. This arrangement promotes the orbital ordering of the Mn^{3+} Jahn-Teller cations in a very stable structure. Recent theoretical studies [9,10] indicate that the very low oxygen conductivity displayed by this phase is related to the strong tendency of high-spin Mn^{3+} to sustain the pyramidal arrangement of atoms, thus, impeding the diffusion of vacancies and/or O^{2-} anions. Additionally, the consistent observations of exact $Sr_2Mn_2O_5$ stoichiometry (oxygen ordered $Sr_2Mn_2O_{5+\delta}$ have never been reported) indicate that the addition of oxygen atoms at the vacant sites with the subsequent formation of Mn^{4+} cations is energetically unfavorable for that phase.

In previous neutron powder diffraction studies, antiferromagnetic ordering of Mn^{3+} magnetic moments has been suggested [6,7] and calculated [9] for $Sr_2Mn_2O_5$. However, the exact magnetic symmetry of $Sr_2Mn_2O_5$ remains uncertain because different magnetic models have been proposed and used [6,7].

On the other hand, high resolution electron microscopy studies demonstrated the existence of at least four vacancy-ordered low oxygen content manganites in the analogous $CaMnO_x$ system [11] with $2.5<x<2.8$. Thus, it is highly probable that similar unidentified oxygen deficient phases are also present in the $SrMnO_x$ system. For example, a recent conference communication [12] reports the isolation of a single crystal of $SrMnO_{2.6}$ with the $A_5Cu_5O_{13+\delta}$ structure type [13] but to the best of our knowledge no complete structural report has been published.

As part of a systematic study of mixed conductors showing fast oxygen conductivity based on bulk substituted strontium manganites, we have synthesized a set of polycrystalline samples with oxygen contents varying from $x = 2.5$ to 2.7 and studied their structural properties using high resolution neutron time-of-flight (TOF) high-energy high-resolution synchrotron X-ray powder diffraction. In this paper, we revisit the nuclear structure of $Sr_2Mn_2O_5$ and we report its correct magnetic structure, confirm the existence of $SrMnO_{2.6}$ ($Sr_5Mn_5O_{13}$) phase, and report the identification of a new oxygen-vacancy ordered phase with an average composition $SrMnO_{2.714}$ corresponding to the formula $Sr_7Mn_7O_{19}$.

2. Experimental procedures

2.1. Sample preparation and experimental procedures

Five batches of $SrMnO_x$ ($x = 2.5$, 2.570(5), 2.595(5), 2.634(5) and 2.668(5)), were prepared by reduction of pure cubic perovskite $SrMnO_3$ starting materials. $SrMnO_3$ sample was prepared using a two-step method previously developed for similar metastable compounds [14–16]. Evolution of the phases during synthesis was checked by room temperature X-ray powder diffraction using a Rigaku D/MAX diffractometer with Ni filtered CuK_α radiation.

Heating of the cubic $SrMnO_3$ material, in a ~50% H_2/Ar flow in a Cahn TG171 thermobalance, produced significant oxygen loss starting at ~200 °C. The oxygen loss continued upon heating until a plateau, corresponding to a composition close to $SrMnO_{2.5}$ ($Sr_2Mn_2O_5$), was observed at 400 °C. Beyond that point, further reduction of the oxygen content lead to the decomposition of the perovskite phase to $Sr_2MnO_{3.5}$ and MnO, and the final formation of SrO and MnO by-products as shown in Fig. 1. Although low-temperature reduction could be used to obtain the $Sr_2Mn_2O_5$ phase (corresponding to an oxygen content of $x = 2.5$), the homogeneity of the sample is poor. In order to obtain high-quality homogeneous crystalline material, we chose an alternative high-temperature method based on the results of the low temperature reductions. A roughly 3 g pellet of $SrMnO_3$ was reduced in a thermobalance to $SrMnO_{2.5}$ at 1300 °C in flowing H_2/Ar (approximately 0.33%H_2). Subsequently, the sample was reground and fired in the thermobalance at 1300 °C in inert gas to ensure equilibrium conditions with no change in oxygen content. The high sample quality was initially checked by conventional X-ray powder diffraction and ultimately confirmed by neutron TOF diffraction experiments performed at various temperatures where less than 2% weight of $Sr_5Mn_5O_{13}$ phase was detected. The sample will be labeled E in subsequent discussion.

About 10 *g* of $SrMnO_3$ was refired in Ar at 1400 °C to obtain an oxygen-deficient sample of approximate

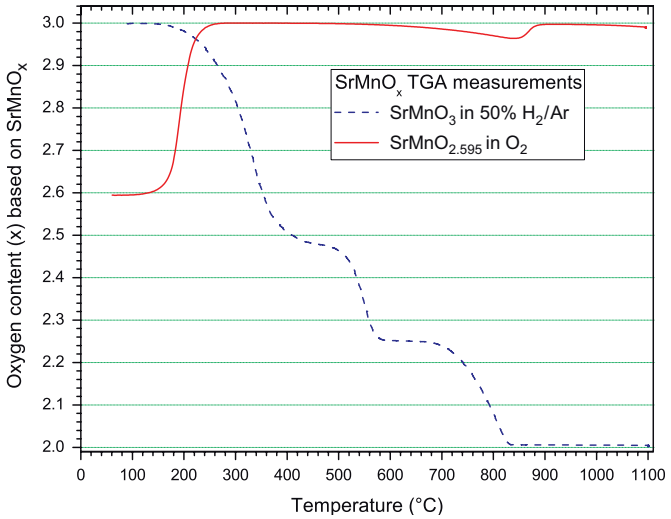

Fig. 1. Thermogravimetric reduction of perovskite $SrMnO_3$ in 50% H_2/Ar gas mixture (broken line) and oxidation of sample B ($SrMnO_{2.595}$) in O_2 (full line) during heating at 1°/min. The reduction of $SrMnO_3$ shows 3 plateaus at $x \approx 2.48$, 2.25 and 2.0 corresponding to the compositions $Sr_2Mn_2O_5$, $Sr_2MnO_{3.5}+MnO$ and $SrO+MnO$ respectively. Oxygen uptake of sample B starts at ~180 °C yielding cubic $SrMnO_3$, which is stable up to ~550 C where the formation of oxygen vacancies is observed. At ~850 °C the conversion of the cubic perovskite to hexagonal four-layered $SrMnO_{3-\delta}$ phase is observed by oxygen uptake to yield α-$SrMnO_3$.

composition $SrMnO_{2.7}$. The sample was divided into four smaller samples that were subsequently reduced using the thermogravimetric balance at 1350 °C in ~0.33% H_2/Ar flow for different periods of time, and followed by stabilization in inert gas, to achieve final oxygen contents of 2.570, 2.595, 2.634, and 2.668 after cooling to room temperature. The four samples will be labeled A, B, C and D, respectively, in following discussion. The final oxygen content of the reduced materials was determined by oxidizing small parts of the samples in O_2 to $SrMnO_{3.000(5)}$ at 500 °C (as shown in Fig. 1 for sample B). None of the four oxygen deficient samples could be considered to be in thermodynamic equilibrium with the flowing gas. Room temperature X-ray diffraction patterns of samples A, B and C revealed the presence of $Sr_2Mn_2O_5$ and two new phases as described herein ($Sr_5Mn_5O_{13}$ and $Sr_7Mn_7O_{19}$) while sample D contains the two new phases with no trace of $Sr_2Mn_2O_5$. X-ray diffraction patterns of all the oxidized samples invariably turned out to be single-phase cubic perovskite $SrMnO_3$ confirming that the new phases are of the perovskite-type and differ only in oxygen content and vacancy ordering schemes.

Neutron TOF room temperature (293(1) K) diffraction data were collected for samples A–D, and between 40 and 450 K for sample E, at the Special Environment Powder Diffractometer (SEPD) at Argonne's Intense Pulsed Neutron Source (IPNS) [17]. High-energy, high-resolution synchrotron X-ray powder diffraction data were collected for samples A–D, at 11-ID-C station (BESSRC-CAT) at Argonne's Advanced Photon Source. A 1 mm thick piece, from each of the pelletized samples, was placed in the beam path inside a mylar film envelope. Data was collected at RT (293(1) K) using hard X-rays, with $\lambda = 0.107634(5)$ Å, in the range $0.7° \leqslant 2\theta \leqslant 8°$ with a step size of 0.001° and a counting time of 1.5 s/step.

2.2. Rietveld structural refinement details

The high-resolution backscattering data bank ($2\theta = 144°$, Bank 1) was used for structural refinements by the Rietveld method with the GSAS/EXPGUI suite of programs [18,19]. For samples D and E, the medium resolution high d-spacing (low q) data bank ($2\theta = 44°$, Bank 3) was also used. A set of routines for sequential refinements by Chmaissem O. (unpublished) were used to analyze the temperature dependent data for sample E. A multi-pattern refinement procedure combining neutron and X-ray data was applied for samples A–D. In all refinements, the background was modeled using a shifted Chebyschev polynomial and the profile function was modeled using the modified Thomson–Cox–Hasting pseudo-Voigt function (TCHZ). For the neutron data, the TCHZ function was convoluted with two back-to-back exponentials to model the intrinsic TOF profile shape. Absorption correction parameter and a zero point error were refined for the neutron and X-ray patterns, respectively. The accurately determined X-ray wavelength was used as a reference for the refinements of unit cell dimensions of all phases. Atomic coordinates and thermal parameters of all the atoms in the phases present in the patterns with weight percentage above 20% were freely refined including anisotropic thermal parameters for O atoms in sample E patterns. Constraints were applied on thermal parameters of $Sr_7Mn_7O_{19}$ phase and minority phases in the different patterns to avoid unphysical values.

3. Results and discussion

Fig. 2 contains five regions of the normalized synchrotron X-ray diffraction patterns showing the evolution of peak positions and relative intensities as a function of increasing oxygen content (i.e., A–D samples). The low q (high d-spacing) region of the patterns (top panel) shows the presence of three sets of reflections and superstructure peaks (with respect to the simple cubic perovskite) depending on the oxygen content. The main peaks observed in the A–C samples with lowest oxygen-content belong to the $Sr_2Mn_2O_5$ and $Sr_5Mn_5O_{13}$ phases. Peaks of $Sr_2Mn_2O_5$ decrease in intensity with increasing x. Peaks belonging to the new $Sr_7Mn_7O_{19}$ phase (not present in sample A) grow in intensity as a function of increasing oxygen content of the samples, consistently with the higher oxygen content of this phase.

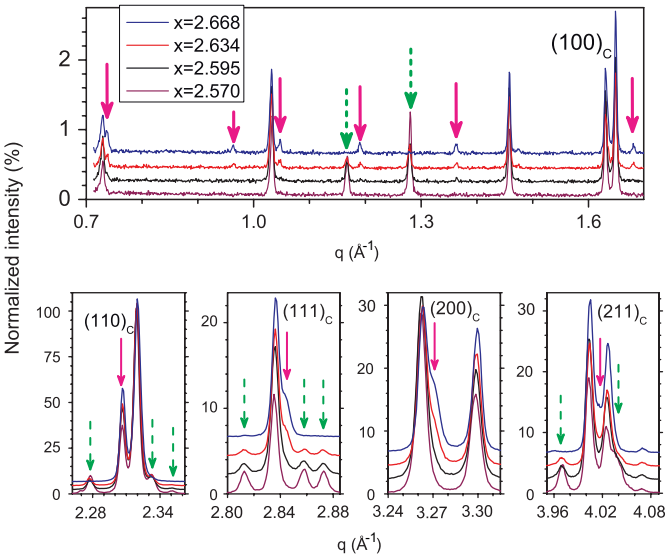

Fig. 2. Selected regions of the normalized high-energy high-resolution synchrotron X-ray powder diffraction patterns for samples A–D. Dashed and solid arrows indicate peaks belonging to $Sr_2Mn_2O_5$ and $Sr_7Mn_7O_{19}$ respectively. Peaks belonging to, or overlapping with, those of $Sr_5Mn_5O_{13}$ are not marked. The $(h\,k\,l)_C$ notation indicate the Miller indices for a cubic perovskite phase. The scale shown in the left corresponds to the normalized intensity (percent) for sample A (bottom pattern). The normalized intensities for samples B–D were displaced vertically for clarity.

3.1. Confirmation of the existence of the tetragonal $Sr_5Mn_5O_{13}$ phase

Both the X-ray and neutron diffraction patterns for sample A were initially fitted with a two-phase structural model containing $Sr_2Mn_2O_5$ and $Sr_5Mn_5O_{13}$. Initial sets of atomic coordinates were extracted from [6,12], respectively. Successful Rietveld structural refinements (see Table 1 for refinement residuals and Fig. 3 for the fitted pattern) confirm the previously reported preliminary results [12] describing a tetragonal $P4/m$ model with approximate unit cell dimensions $a_T \approx b_T \approx \sqrt{5} * a_C$ and $c_T \approx a_C$ for the $Sr_5Mn_5O_{13}$ (or $SrMnO_{2.6}$) phase. The observation of peaks that originate from the magnetic ordering of $Sr_2Mn_2O_5$ required further analysis as discussed in Section 3.3. For both phases, partial occupancy of the vacant sites was refined with results discussed in Section 3.4. A reliable structural model for the $Sr_5Mn_5O_{13}$ phase (Table 2) was obtained from fits to the data for sample B that contained the highest amount of this new phase. Structural details will be discussed in Section 3.4.

3.2. Determination of the monoclinic structure of $Sr_7Mn_7O_{19}$

The structure of the $Sr_7Mn_7O_{19}$ phase was determined by analogy with $Sr_5Mn_5O_{13}$. Cell parameters were obtained through an auto-indexing procedure using peak positions extracted from the difference curve of the synchrotron X-ray pattern of sample D fitted with only the tetragonal $Sr_5Mn_5O_{13}$ phase. The positions of a total of 29 unindexed peaks were determined using the program PowderX [20]. Dicvol04 [21] indexing software was used to obtain a solution for all 29 input reflections in the monoclinic system with figures of merit $M(29) = 5.9$ and $F(29) = 48.1(0.0008,769)$. It should be noted that the relatively low figures of merit can be explained by the significant overlap between peaks from the new $Sr_7Mn_7O_{19}$ phase and $Sr_5Mn_5O_{13}$ which prevented the use of many major peaks in the indexing procedure. The unit cell of the new phase was later confirmed and refined using the LeBail method [22] (as implemented in GSAS) on the synchrotron X-ray pattern in which the $Sr_5Mn_5O_{13}$ structure was refined in a Rietveld mode. Analysis of systematic absences to determine the space group of the new phase limited the possible space groups to $P2_1/m$ or $P2/m$ (cell choice 2) [23]. Space group $P2_1/m$ was ruled out because of the absence of 2_1 fold symmetry axes parallel to c in the cubic $SrMnO_3$, orthorhombic $Sr_2Mn_2O_5$ or tetragonal $Sr_5Mn_5O_{13}$ phases (all with $c \approx a_C$). The $P2/m$ space group resulted in excellent fits to the combination of the synchrotron X-ray and neutron (Banks 1 and 3) data and was adopted thereafter.

The unit cell dimensions of $Sr_7Mn_7O_{19}$ could be correlated with those of the original perovskite-type cubic cell. If $\vec{a}_P$, $\vec{b}_P$ and $\vec{c}_P$ were the three vectors (100), (010) and (001) of a simple cubic perovskite all with modulus $\mathbf{a}_P$, then $\vec{a}_M \approx -\vec{a}_P + 2\vec{b}_P$, $\vec{b}_M \approx \vec{b}_P + 3\vec{a}_P$ and $\vec{c}_M \approx \vec{c}_P$ with moduli $\mathbf{a}_M \approx \sqrt{5} * \mathbf{a}_P$, $\mathbf{b}_M \approx \sqrt{10} * \mathbf{a}_P$ and $\mathbf{c}_M \approx \mathbf{a}_P$, respectively, and with $\gamma \approx 180 - \text{arctg}(2b_P/a_P) - \text{arctg}(b_P/3a_P) = 98.13^\circ$. A unit cell composition of $Sr_7Mn_7O_{21-N}$ (integer N is the number of vacant oxygen sites) was suggested by the refined unit cell volume $V = 395.024\,\text{Å}^3$ which is approximately seven times larger than that of cubic $SrMnO_3$ ($V_C = 55.049\,\text{Å}^3$ [16]) and in the ratio of $\sim 7/5$ with respect to the unit cell volume of $Sr_5Mn_5O_{13}$.

According to the thermogravimetric oxygen measurements for sample D ($SrMnO_{2.668}$), the oxygen content of the new phase is expected to be in the range $2.7 < x < 2.9$ (or $0.7 < N < 2.1$) depending on the weight percentage ratio of $Sr_7Mn_7O_{21-N}$ and $Sr_5Mn_5O_{13}$. The refinement of models with $N = 1$ ($Sr_7Mn_7O_{20}$ or $SrMnO_{2.857}$) and $N = 2$ ($Sr_7Mn_7O_{19}$ or $SrMnO_{2.714}$) clearly favored the latter. However, weight percentages of the $Sr_5Mn_5O_{13}$ and $Sr_7Mn_7O_{19}$ phases extracted from the fit of the patterns

Table 1
Refinement residuals and weight percentages of $Sr_2Mn_2O_5$, $Sr_5Mn_5O_{13}$ and $Sr_7Mn_7O_{19}$ in samples A, B, C, D and E (300 K data only) after Rietveld fit of the corresponding patterns

Sample	$SrMnO_x$		Refinement residuals (%)				Weight percentages		
	(x)		χ^2	R_p	R_{wp}	$R(F^2)$	$Sr_2Mn_2O_5$	$Sr_5Mn_5O_{13}$	$Sr_7Mn_7O_{19}$
A	2.570	X-R	2.132	7.56	10.63	3.40	37(1)	63(1)	—
		N-B1		4.09	5.55	4.28			
B	2.595[a]	X-R	2.088	6.90	9.60	3.92	18(2)	70(2)	12(2)
		N-B1		6.03	8.67	4.55			
C	2.634[a]	X-R	2.424	8.10	11.22	6.00	12(2)	58(2)	30(2)
		N-B1		6.38	8.90	9.32			
D	2.668	X-R	2.515	9.07	12.11	6.71	—	62(1)	38(1)
		N-B1		7.09	9.96	6.46			
		N-B3		5.26	7.36	6.20			
E	2.5	N-B1	1.291	4.14	6.72	3.45	98(1)	2(1)	—
		N-B3		3.74	6.28	3.36			

X-R stands for X-rays, N-B1 for neutrons Bank 1 and N-B3 for neutrons Bank 3.
[a]The scattering from the magnetic arrangement in $Sr_2Mn_2O_5$ visible in the NPD was disregarded in this refinement.

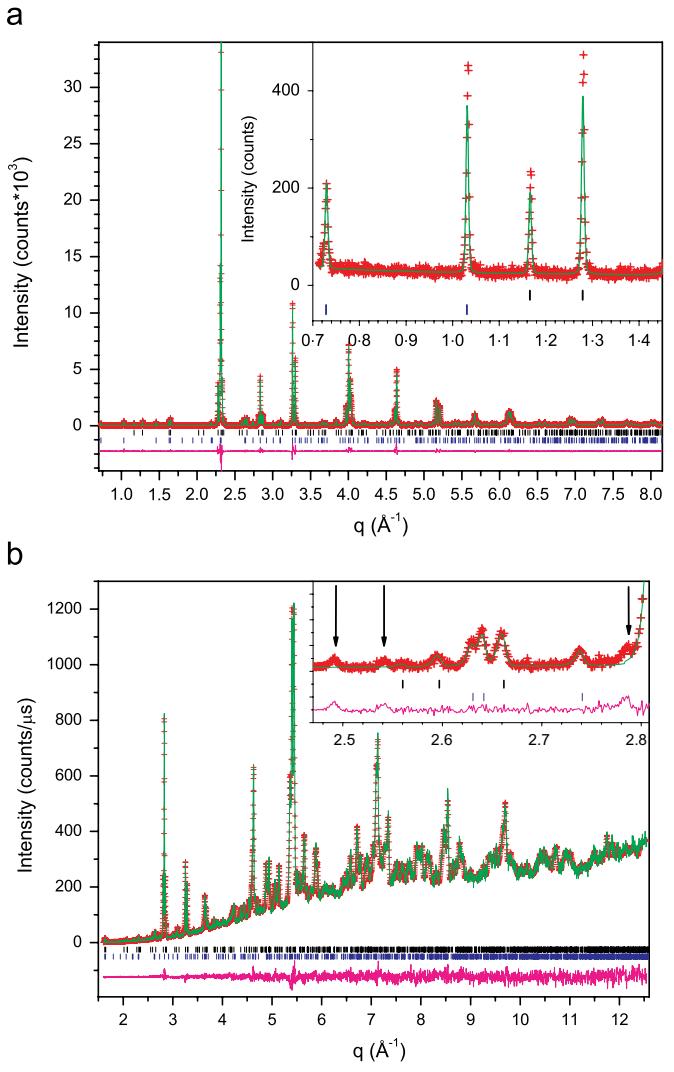

Fig. 3. Final fits of the X-ray (top) and neutron (bottom) patterns for sample A including phases $Sr_2Mn_2O_5$ in P_cbam (see Section 3.3) and $Sr_5Mn_5O_{13}$ (top and bottom row of tick-marks, respectively). The inset in the top panel shows the fit of the low q region of the X-ray pattern. The inset in the lower panel shows a region of the pattern where the magnetic peaks are not fitted (arrows) before including a magnetic model for $Sr_2Mn_2O_5$ in the refinement.

for sample D do not reproduce the global oxygen content of the sample, thus suggesting the presence of non-stoichiometric oxygen in the vacant sites, for the new phase. The final refined structural parameters shown in Table 2 correspond to $Sr_7Mn_7O_{19.33}$ phase. Structural details will be discussed in Section 3.4.

After the structure of the high-oxygen content phase was determined, the final fits of the patterns for samples B and C resulted in very low residual factors and consistent relations between the three observed phases $Sr_2Mn_2O_5$, $Sr_5Mn_5O_{13}$ and $Sr_7Mn_7O_{19}$ (see Table 1). Figs. 4 and 5 show fitted patterns for samples B and D and Fig. 6 shows the final structural models for $Sr_2Mn_2O_5$, $Sr_5Mn_5O_{13}$ and $Sr_7Mn_7O_{19}$ phases. In $Sr_5Mn_5O_{13}$ and $Sr_7Mn_7O_{19}$ structures, the a-axis corresponds to the distance between two octahedra with a vacant site between them which explains the similarity in dimensions. Presence of the three phases in B and C samples is in agreement with the non-equilibrium synthesis conditions as discussed in Section 2.1.

3.3. The correct magnetic structure of $Sr_2Mn_2O_5$

In previous work, Caignaert [6] reported the nuclear and magnetic structures of $Sr_2Mn_2O_5$ determined using neutron powder diffraction. Refinements of the nuclear and magnetic structures were carried out in the *Pbam* and *P*1 space group symmetries, respectively. Thus, two magnetic structural models (G_xA_y and F_xC_y) have been identified as possible solutions. However, considering the oxidation state of Mn, internal bond-lengths and angles, in addition to other geometrical considerations, the G_xA_y magnetic model in a P_cbam symmetry setting (using Shubnikov notation [24]) was selected. In this model, the Mn^{3+} moments order antiferromagnetically with refined magnetic moment components $\mu_x = 0.5(2)\,\mu_B$ and $\mu_y = 2.57(4)\,\mu_B$ at 4.2 K. Two consecutive Mn layers perpendicular to the z direction display opposite spin directions, thus, a doubled magnetic unit cell, with respect to the nuclear one, should be adopted.

In another study, Mori et al. [7] described the global nuclear and magnetic structures of this compound using the *Pnnm* space group and a super-cell of dimensions $a' = a$, $b' = b$ and $c' = 2*c$. The coordinates of certain atoms were fixed at positions where no special symmetry exist, and only the y-component of the magnetic moment ($\mu_y = 3.44\,\mu_B$ at 20 K) was refined (defining a simpler A_y model) with no details of the magnetic symmetry reported.

In the present study, combined nuclear and magnetic structural refinements for $Sr_2Mn_2O_5$ were performed using bicolor symmetry operators included in GSAS. We have determined that the model described by Mori et al. is equivalent to the P_cbam Shubnikov symmetry used by Caignaert when the coordinates of the magnetic atoms are constrained to display the same site symmetry in both the nuclear and magnetic cells (except for the refinement of only one component of the magnetic moment as stated above). Moreover, we find that two additional models can be built based on the *Pbam* and *Pbnm* nuclear space groups (*Pbnm* is a non-conventional representation of the *Pnma* space group [23]) with $c' = 2*c$ that provide exactly the same magnetic structure when proper constraints on the coordinates and bicolor symmetry operators have been applied. This observation can be explained by the group–subgroup relation between the *Pbam* space group (with cell dimensions a, b, c) and the *Pbam*, *Pnnm* and *Pbnm* space groups with the unit cells doubled in the c-axis direction (or $a' = a$, $b' = b$ and $c' = 2*c$) as can be extracted from [23] together with the fact that Mn^{3+} cations occupy the 4g Wyckoff special symmetry positions (over a mirror plane) in the unit cell. Additionally, the orientation of the moments with the main component lying along the y-axis

Table 2
Refined structural parameters for the phase $Sr_2Mn_2O_5$ in sample *E* (300(1) K) $Sr_5Mn_5O_{13}$ in the sample B and $Sr_7Mn_7O_{19}$ in sample D both at 293(1) K

$Sr_2Mn_2O_5$ (nuclear structure)

Orthorhombic, *Pbam*(#55), $a = 5.5171(2)$ Å, $b = 10.7722(4)$ Å, $c = 3.8091(2)$ Å, $V = 226.38(2)$ Å^3

Name	Ion	Wyckoff	x	y	z	$U_{11/iso}$ ($\times 100$ Å^2)	U_{22} ($\times 100$ Å^2)	U_{33} ($\times 100$ Å^2)	U_{12} ($\times 100$ Å^2)
Sr1	Sr^{2+}	4*h*	0.2896(2)	0.3650(2)	$\frac{1}{2}$	0.57(3)	—	—	—
Mn1	Mn^{3+}	4*g*	0.2596(4)	0.1217(2)	0	0.30(4)	—	—	—
O1	O^{2-}	4*h*	0.2859(3)	0.1037(2)	$\frac{1}{2}$	1.27(8)	1.05(8)	0.02(6)	−0.20(7)
O2	O^{2-}	4*g*	0.5297(3)	0.2273(2)	0	0.69(70	0.88(9)	0.39(9)	−0.33(6)
O3	O^{2-}	2*a*	0	0	0	0.9(2)	0.9(2)	0.3(2)	−0.51(8)

$Sr_5Mn_5O_{13.19}$

Tetragonal, *P*4/*m*(#83), $a = 8.6127(3)$ Å, $c = 3.8102(2)$ Å, $V = 282.64(2)$ Å^3

Name	Ion	Wyckoff	x	y	z	U_{iso} ($\times 100$ Å^2)	SOF
Sr1	Sr^{2+}	1*d*	$\frac{1}{2}$	$\frac{1}{2}$	$\frac{1}{2}$	0.88(5)	1
Sr2	Sr^{2+}	4*k*	0.1148 (2)	0.7172(2)	$\frac{1}{2}$	0.47(2)	1
Mn1	Mn^{4+}	1*a*	0	0	0	0.27(7)	1
Mn2	Mn^{3+}	4*j*	0.1956(2)	0.4007(2)	0	0.46(3)	1
O1	O^{2-}	1*b*	0	0	$\frac{1}{2}$	0.5(2)	1
O2	O^{2-}	4*k*	0.1686(4)	0.4107(5)	$\frac{1}{2}$	0.68(8)	1
O12	O^{2-}	4*j*	0.0733(5)	0.2118(5)	0	0.53(6)	1
O22	O^{2-}	4*j*	0.4041(4)	0.2840(5)	0	0.74(8)	1
O_δ	O^{2-}	2*e*	1/2	0	0	0.6	0.09(1)

$Sr_7Mn_7O_{19.33}$

Monoclinic, *P*2/*m* (#10), $a = 8.6076(4)$ Å, $b = 12.1284(4)$ Å, $c = 3.8076(2)$ Å, $\gamma = 98.203(2)^\circ$, $V = 393.43(3)$ Å^3

Name	Ion	Wyckoff	x	y	z	U_{iso} ($\times 100$ Å^2) [a]	SOF
Sr1	Sr^{2+}	1*e*	0	$\frac{1}{2}$	$\frac{1}{2}$	0.39(4)	1
Sr2	Sr^{2+}	2*n*	0.1474(5)	0.2160(4)	$\frac{1}{2}$	0.39(4)	1
Sr3	Sr^{2+}	2*n*	0.7308(5)	0.0743(4)	$\frac{1}{2}$	0.39(4)	1
Sr4	Sr^{2+}	2*n*	0.5780(5)	0.3436(4)	$\frac{1}{2}$	0.39(4)	1
Mn1	Mn^{4+}	1*a*	0	0	0	0.39(4)	1
Mn2	Mn^{4+}	2*m*	0.8641(8)	0.2881(7)	0	0.39(4)	1
Mn3	Mn^{3+}	2*m*	0.4266(9)	0.1428(6)	0	0.39(4)	1
Mn4	Mn^{3+}	2*m*	0.2894(9)	0.4312(6)	0	0.39(4)	1
O1	O^{2-}	1*b*	0	0	$\frac{1}{2}$	0.60(8)	1
O2	O^{2-}	2*n*	0.854(3)	0.283(2)	$\frac{1}{2}$	0.60(8)	1
O3	O^{2-}	2*n*	0.436(3)	0.129(2)	$\frac{1}{2}$	0.60(8)	1
O4	O^{2-}	2*n*	0.302(3)	0.438(2)	$\frac{1}{2}$	0.60(8)	1
O12	O^{2-}	2*n*	−0.060(3)	0.146(2)	0	0.60(8)	1
O13	O^{2-}	2*n*	0.226(3)	0.058(2)	0	0.60(8)	1
O23	O^{2-}	2*n*	0.654(3)	0.191(2)	0	0.60(8)	1
O24	O^{2-}	2*n*	0.061(3)	0.364(2)	0	0.60(8)	1
O34	O^{2-}	2*n*	0.358(3)	0.292(2)	0	0.60(8)	1
O42	O^{2-}	2*n*	0.766(3)	0.418(2)	0	0.60(8)	1
$O_{\delta1}$	O^{2-}	1*c*	$\frac{1}{2}$	0	0	0.6	0.13(4)
$O_{\delta2}$	O^{2-}	1*g*	$\frac{1}{2}$	$\frac{1}{2}$	0	0.6	0.19(5)

[a]The thermal parameters of Sr/Mn and O atoms were constrained to be equal to avoid unrealistic values.

direction reinforces the special symmetry of this structure leading to multiple possible and equivalent representations of the magnetic symmetry. Thus, only the determination of which of the two possible moment configurations G_xA_y or A_y is best in a P_cbam Shubnikov space group was needed to determine the correct magnetic structure.

A set of initial refinements was performed using the data collected between 40 and 450 K and the P_cbam magnetic

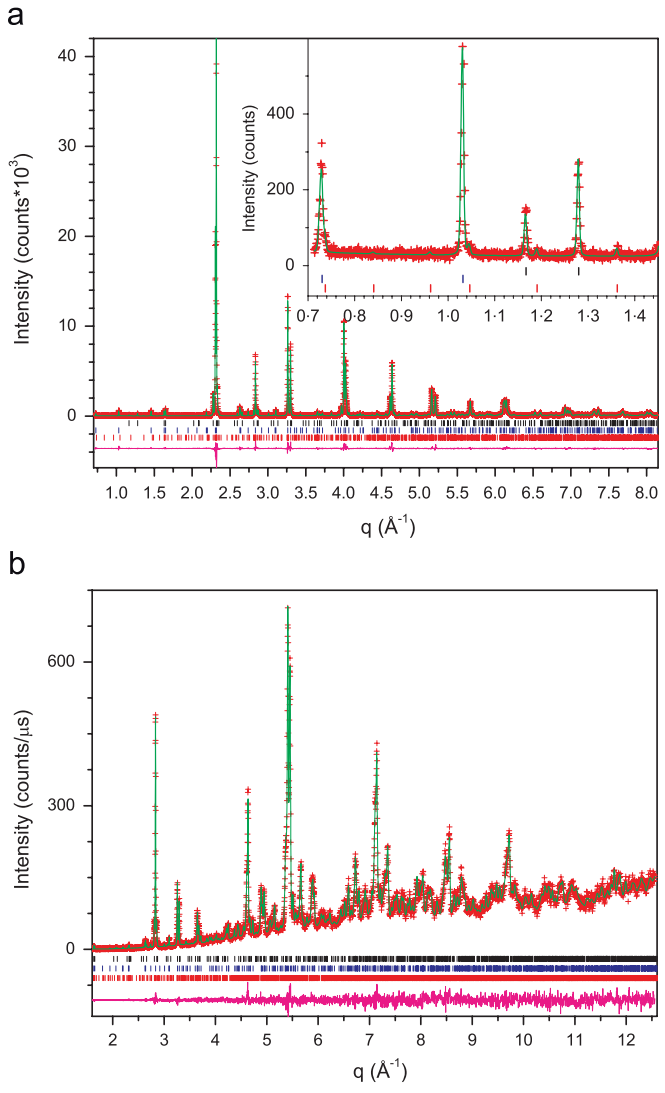

Fig. 4. Final fits of the X-ray (top) and neutron (bottom) patterns for sample B including phases $Sr_2Mn_2O_5$, $Sr_5Mn_5O_{13}$ and $Sr_7Mn_7O_{19}$ (top, middle and bottom row of tick-marks, respectively). The inset in the top panel shows the fit of the low q region of the X-ray pattern.

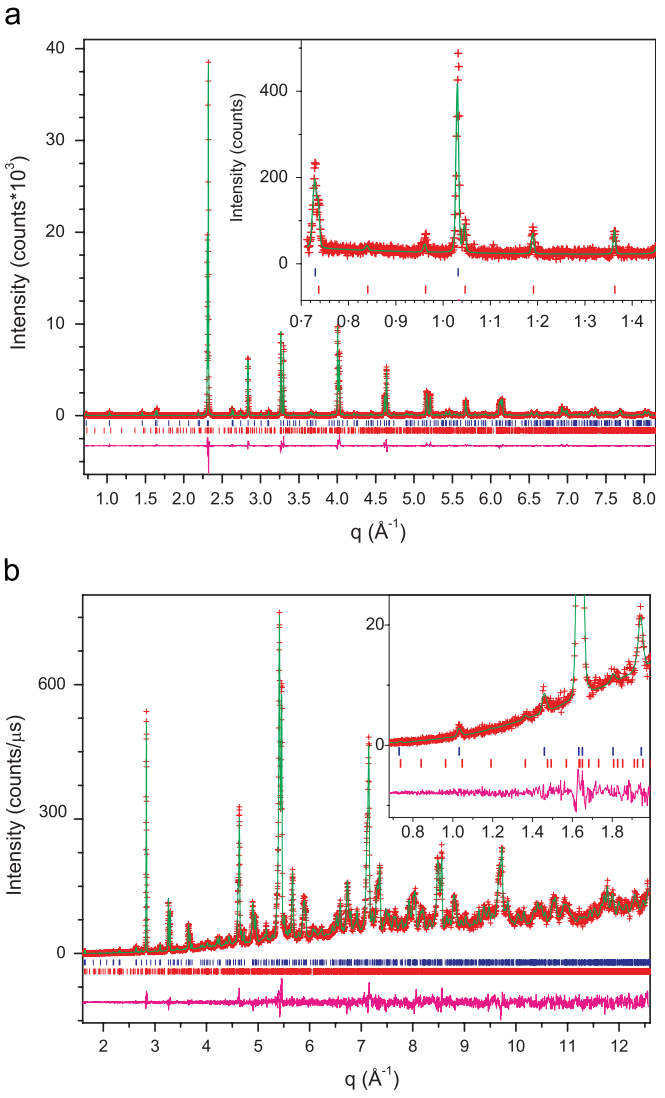

Fig. 5. Final fits of the X-ray (top) and neutron (bottom) patterns for sample D including phases $Sr_5Mn_5O_{13}$ and $Sr_7Mn_7O_{19}$ (top and bottom row of tick-marks, respectively). The insets in both panels show the fit of the low q region of the patterns (a region of Bank 3 in the neutron data). The relative intensity of the superstructure peaks for X-ray and neutrons is evident in this figure.

symmetry (the fitted 40 K pattern is shown in Fig. 7) allowing both the x and y components of the Mn magnetic moment to refine. The μ_y component decreased with increasing temperature up to the Neel temperature where it stabilized in a null value (within experimental error) as shown in Fig. 8a; however, the μ_x component appears to be constant with a value of $\sim 0.3(1)\,\mu_B$ within the studied temperature range, even at 450 K (well above $T_N \sim 380$ K). The paramagnetic properties for this sample above 380 K lead us to conclude that this non-zero μ_x component is due to an artifact of the refinement and falls below the instrument resolution limit. A second set of refinements was performed including only the y-component of the magnetic moment with equivalent results, as shown in Fig. 8b. We, therefore, conclude that the A_y moment configuration in a P_cbam space group symmetry is the correct magnetic symmetry for $Sr_2Mn_2O_5$.

3.4. *Structural trends, orbital and charge ordering, oxygen non-stoichiometry and miscibility gaps in the $SrMnO_x$ system ($2.5 < x < 2.7$).*

Several features are shared among the three oxygen-vacancy ordered phases observed in the $SrMnO_x$ system. For the three of them, oxygen vacancies are aligned along one of the cubic 1 0 0 direction defining the crystallographic c-axis (Fig. 6). Pseudo-hexagonal channels are formed around the vacant oxygen site where ten-coordinated Sr^{2+} cations are located in the three structures, but extra twelve-coordinated sites exist for Sr^{2+} in $Sr_5Mn_5O_{13}$ (1 site) and $Sr_7Mn_7O_{19}$ (2 sites). This vacancy ordering promotes charge ordering of Mn^{3+} and Mn^{4+} cations in pyramidal and octahedral coordination respectively for both $Sr_5Mn_5O_{13}$ and $Sr_7Mn_7O_{19}$. The observed average charges

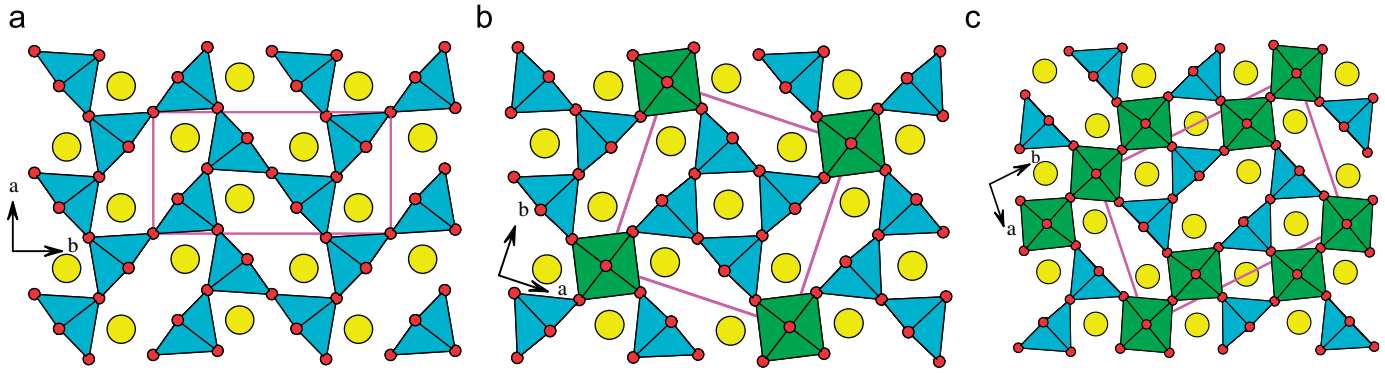

Fig. 6. Crystal structures of $Sr_2Mn_2O_5$ (top), $Sr_5Mn_5O_{13}$ (middle), and $Sr_7Mn_7O_{19}$ (bottom) viewed along 0 0 1 direction. Octahedra correspond to Mn^{4+} and pyramids to Mn^{3+} cations. O^{2-} are shown as small dark circles and Sr^{2+} cations as big light circles. Partially occupied oxygen sites are shown vacant for clarity.

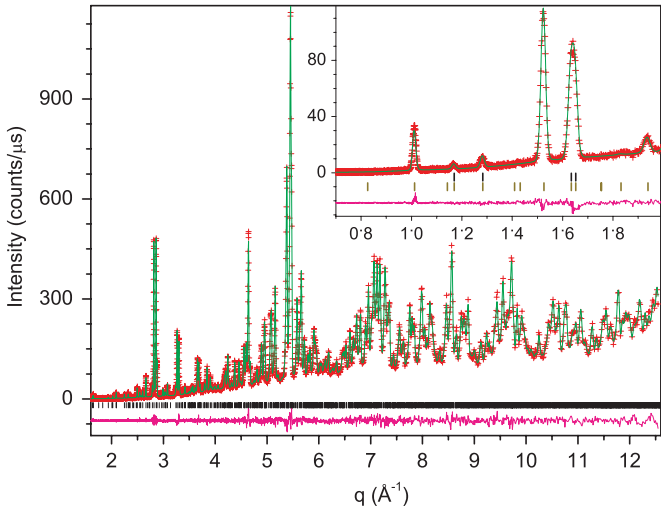

Fig. 7. Fitted neutron patterns of $Sr_2Mn_2O_5$ (sample E) at 40 K using the P_cbam symmetry model and the *Ay* arrangement of moments. The inset shows a detail of the low *q* data (Bank 3). The purely structural peaks are shown in the top row of tick-marks while the magnetic ones in the bottom row.

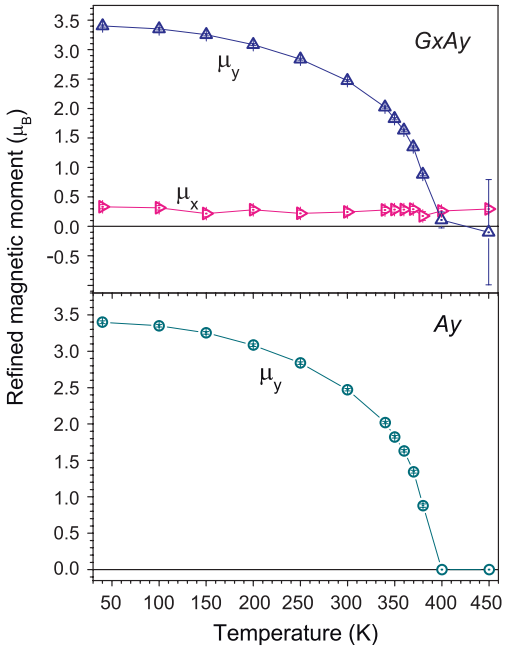

Fig. 8. Magnetic moments of Mn atoms in $Sr_2Mn_2O_5$ in a: *GxAy* (top) and b: *Ay* (bottom) models (see text). Error bars are in most cases smaller than symbol size. The value of the magnetic moment at temperatures above T_N was fixed to 0 in the final *Ay* model to avoid correlation with structural parameters. The lines are guides to the eye.

$Mn^{(16/5)+}$ in $Sr_5Mn_5O_{13}$ and $Mn^{(24/7)+}$ in $Sr_7Mn_7O_{19}$ comply with Mn^{3+}/Mn^{4+} ratios that allow description of both charge ordered compounds as $Sr_5Mn^{4+}(Mn^{3+})_4O_{13}$ and $Sr_7(Mn^{4+})_3(Mn^{3+})_4O_{19}$ respectively.

The increasing complexity of the structures with oxygen content forces each pyramid to be connected in the *ab* plane with three other pyramids in $Sr_2Mn_2O_5$, two pyramids and one octahedra in $Sr_5Mn_5O_{13}$, and only one pyramid and two octahedra in $Sr_7Mn_7O_{19}$. However, the orbital ordering of pyramidal Mn^{3+} cations described in $Sr_2Mn_2O_5$ [6] is also present in both $Sr_5Mn_5O_{13}$ and $Sr_7Mn_7O_{19}$, as can be clearly extracted from the Mn–O bond distances and angles listed in Table 3. Particularly, the Mn2 atoms in $Sr_5Mn_5O_{13}$ and Mn3 and Mn4 atoms in $Sr_7Mn_7O_{19}$ share a common pyramidal shape with one elongated, one short, and three intermediate Mn–O bonds. In all cases, as in $Sr_2Mn_2O_5$, the long Mn–O bond is in the apical direction of the pyramid while the intermediate and short bonds are in the equatorial directions. The apical oxygen atom from one pyramid forms a short Mn–O bond with a neighboring one except for the apical atom O24 in the Mn4 pyramid of $Sr_7Mn_7O_{19}$ which is shared with Mn2 octahedra, not pyramids. However, the Mn2–O24 bond in the octahedra is just as short as those observed in the pyramids. At the same time, the existence of regular octahedra in $Sr_5Mn_5O_{13}$ and $Sr_7Mn_7O_{19}$ clearly indicates the presence of Mn^{4+}, which is not a Jahn-Teller ion, providing additional evidence of charge ordering in both compounds.

The possibility of finding non-stoichiometric oxygen in the vacant sites of the new phases was considered during the structural refinements. For $Sr_2Mn_2O_5$, neither the previous studies [5–7] nor our refinements show non-stoichiometric oxygen in the vacant sites. For the $Sr_5Mn_5O_{13}$ phase,

Table 3
Bond distances (Å) and angles (degrees) involving Mn–O polyhedra in $Sr_2Mn_2O_5$, $Sr_5Mn_5O_{13}$ and $Sr_7Mn_7O_{19}$ at room temperature. Additional bond distances for $Sr_2Mn_2O_5$ and $SrMnO_3$ were extracted from [6] and [15] respectively.

$Sr_5Mn_5O_{13}$		$Sr_7Mn_7O_{19}$				$SrMnO_3$	
Mn1		Mn1		Mn2		Mn1	[15]
O1 (× 2)	1.9051(1)	O1 (× 2)	1.9038(1)	O2 (× 2)	1.906(2)	O1 (× 6)	1.90205(15)
O12 (× 4)	1.930(4)	O12 (× 2)	1.91(2)	O12	1.93(2)		
		O13 (× 2)	1.97(2)	O23	2.02(2)		
				O24	1.80(2)		
				O42	1.89(2)		

$Sr_5Mn_5O_{13}$		$Sr_7Mn_7O_{19}$				$Sr_2Mn_2O_5$		
Mn2		Mn3		Mn4		Mn1	This work	[6]
O2 (× 2)	1.9212(5)	O3 (× 2)	1.914(3)	O4 (× 2)	1.908(2)	O1 (× 2)	1.9198(4)	1.919(2)
O12	1.938(5)	O23	1.96(2)	O42	1.96(2)	O3	1.941(3)	1.95(2)
O22a	2.058(4)	O34	1.99(2)	O24	2.02(3)	O2a	2.063(3)	2.06(2)
O22e	1.846(4)	O13	1.88(3)	O34	1.86(2)	O2e	1.875(3)	1.87(2)
O2– –O2	165.2(3)	O3– –O3	168(2)	O4– –O4	172(2)	O1– –O1	165.5(2)	
O2– –O12 (× 2)	88.4(2)	O3– –O23 (× 2)	88.5(7)	O4– –O42 (× 2)	88.8(6)	O1– –O3 (× 2)	89.31(8)	
O2– –O22a (× 2)	97.3(2)	O3– –O34 (× 2)	96.0(6)	O4– –O24 (× 2)	93.7(7)	O1– –O2a (× 2)	97.23(8)	
O2– –O22e (× 2)	90.5(2)	O3– –O13 (× 2)	89.9(7)	O4– –O34 (× 2)	90.9(6)	O1– –O2e (× 2)	90.05(9)	
O12– –O22a	93.7(2)	O23– –O34	98(1)	O42– –O24	91.6(9)	O2a– –O3	94.5(2)	
O12– –O22e	171.5(2)	O13– –O23	164.0(9)	O42– –O34	176(2)	O2e– –O3	174.9(2)	
O22a– –O22e	94.9(3)	O13– –O34	97.8(9)	O24– –O34	93(1)	O2a– –O2e	90.57(8)	

A letter a or e after the atom name (e.g. O22a or O22e) means that the O atom is bonded to the a Mn atom in an apical or equatorial position,respectively.
Bond angles in Mn octahedra were omitted because they do not add to the structural discussion.
Bond distances and angles to non-stoichiometric oxygen atoms were omitted as they do not represent the actual Mn–O bond distance when the vacant site is occupied.

refinement of the partial oxygen occupancy in the vacant site for the four investigated samples is not conclusive due to observation of values that vary between 10% and 25% of non-stoichiometric oxygen depending on the sample. However, it remains unclear if the observed partial occupation of vacant sites is not simply an artifact of the refinement caused by the strong overlap of reflections for the three phases at high q values. In principle, there is no limit on the amount of oxygen that could be accepted in $Sr_7Mn_7O_{19}$, except for the competition with the oxygen disordered orthorhombic and tetragonal phases reported for $x > 2.66$ [2]. Local distortions induced by one filled vacancy causing two Mn^{3+} pyramids to transform into two Mn^{4+} octahedra should cause changes in peak shape and intensity in the diffraction pattern that are not modeled in our refinements and might have an influence in the final observed structural parameters. For both $Sr_5Mn_5O_{13}$ and $Sr_7Mn_7O_{19}$ phases, further studies with single-phase samples should be performed to address this point.

Finally, considering the vacancy arrangements in the three studied compounds and the observation of multiple phases in all the samples with intermediate oxygen contents (x) (i.e., above 2.5 and below 2.7) we propose the existence of two miscibility gaps in the $SrMnO_x$ system. The first one exists between the compositions $SrMnO_{2.5}$ and $SrMnO_{2.6}$ ($Sr_2Mn_2O_5$ and $Sr_5Mn_5O_{13}$) and the second one between $SrMnO_{2.6}$ and $SrMnO_{2.714}$ ($Sr_5Mn_5O_{13}$ and $Sr_7Mn_7O_{19}$).

4. Conclusions

Structural characterization of the mixed valence oxygen-vacancy and charge-ordered $Sr_5Mn_5O_{13}$ ($Sr_5Mn^{4+}(Mn^{3+})_4O_{13}$) and $Sr_7Mn_7O_{19}$ ($Sr_7(Mn^{4+})_3(Mn^{3+})_4O_{19}$) phases in bulk samples was achieved in the tetragonal $P4/m$ and monoclinic $P2/m$ space groups, respectively. These phases were found to coexist with the well-known orthorhombic $Sr_2(Mn^{3+})_2O_5$ in the non-equilibrium samples used for structural determination and refinements. Identical vacancy-ordered phases $La_2Cu_2O_5$ and $La_5Cu_5O_{13}$ have been previously observed for $LaCuO_x$ system with the Jahn-Teller Cu^{2+}, indicating that the simultaneous presence of highly distorted pyramidally coordinated Cu^{2+} (Mn^{3+}) and symmetric octahedrally coordinated Cu^{3+} (Mn^{4+}) leads to a similar ordering schemes for oxygen deficient perovskites. The existence of miscibility gaps between the compositions $SrMnO_{2.5}$, $SrMnO_{2.6}$ and $SrMnO_{2.714}$ could explain their coexistence in the studied samples. The correct magnetic model for $Sr_2Mn_2O_5$ phase was determined in the P_cbam Shubnikov space group with a collinear antiferromagnetic A_y type arrangement of moments in Mn^{3+} cations below T_N.

Efforts to obtain single phase $Sr_5Mn_5O_{13}$ and $Sr_7Mn_7O_{19}$ samples and determine the ability of the structures to accommodate non-stoichiometric oxygen content, their temperature stability ranges and mixed ionic-electronic conductivity, as well as magnetic properties

is being conducted at present and will be published elsewhere.

Supplementary data

Further details of the crystal structure investigations may be obtained from Fachinformationszentrum Karlsruhe, 76344 Eggenstein-Leopoldshafen, Germany (fax: +49 7247 808 666; e-mail: crysdata@fiz-karlsruhe.de, http://www.fiz-karlsruhe.de/ecid/Internet/en/DB/icsd/depot_anforderung.html) on quoting the deposition numbers CSD-417534 ($Sr_7Mn_7O_{19}$), CSD-417535 ($Sr_5Mn_5O_{13}$) and CSD-417806 to 417818 ($Sr_2Mn_2O_5$ 40 to 450 K).

Acknowledgments

Use of the Advanced Photon Source and Intense Pulsed Neutron Source was supported by the US Department of Energy, Office of Science, Office of Basic Energy Sciences, under Contract No. DE-AC02-06CH11357. We wish to thank Dr. Yang Ren for his help with the high-energy high-resolution synchrotron X-ray data collection. Work at NIU was supported by the NSF Grant No. DMR-0302617 and the US Department of Transportation.

References

[1] T. Negas, S.J. Roth, J. Solid State Chem. 1 (1970) 409–418.
[2] R.S. Tichy, J.B. Goodenough, Solid State Sci. 4 (2002) 661–664.
[3] N. Mizutani, A. Kitazawa, N. Ohkuma, M. Kato, Kogyo Kagaki Zasshi 73 (6) (1970) 1097–1103.
[4] K. Kuroda, S. Shinozaki, K. Uematsu, N. Mizutani, M. Kato, Nipon Kagaku Kaishi 11 (1977) 1620–1625.
[5] V. Caignaert, N. Nguyen, M. Hervieu, B. Raveau, Mater. Res. Bull. 20 (1985) 479–484.
[6] V. Caignaert, J. Magn. Magn. Mater. 166 (1997) 117–123.
[7] T. Mori, K. Inoue, N. Kamegashira, Y. Yamaguchi, K. Ohoyama, J. Alloys Compd. 296 (2000) 92–97.
[8] K.R. Poeppelmeier, M.E. Leonowicz, J.C. Scanlon, J.M. Longo, W.B. Yelon, J. Solid State Chem. 45 (1982) 71–79.
[9] S. Stolen, C.E. Mohn, P. Ravindran, N.L. Allan, J. Phys. Chem. B 109 (2005) 12362–12365.
[10] A.N. Grundi, B. Hallstedt, L.J. Gaukler, J. Phase Equilib. Diffus. 25 (2004) 311–319.
[11] A. Reller, J.M. Thomas, D.A. Jefferson, M.K. Uppal, Proc. R. Soc. London A. 394 (1984) 223–241.
[12] H. Leligny, D. Grebille, M. Hervieu, C. Martin, Poster Communication, Association Francaise de Cristallographie, 2003.
[13] S.J. La Placa, J.F. Bringley, B.A. Scott, J. Solid State Chem. 118 (1995) 143–152.
[14] D.G. Hinks, B. Dabrowski, J.D. Jorgensen, A.W. Mitchell, D.R. Richards, D.-L. Shi, Nature (London, UK) 333 (1988) 836–838.
[15] O. Chmaissem, B. Dabrowski, S. Kolesnik, J. Mais, J.D. Jorgensen, S. Short, Phys. Rev. B: Condens Matter Mater. Phys. 67 (2003) 094431.
[16] B. Dabrowski, O. Chmaissem, J. Mais, S. Kolesnik, J.D. Jorgensen, S. Short, J. Solid State Chem. 170 (2003) 154–164.
[17] J.D. Jorgensen, J. Faber Jr., J.M. Carpenter, R.K. Crawford, J.R. Haumann, R.L. Hitterman, R. Kleb, G.E. Ostrowski, F.J. Rotella, T.G. Worlton, J. Appl. Crystallogr. (1989) 321–333.
[18] A.C. Larson, R.B. Von Dreele, General Structure Analysis System (GSAS), Los Alamos National Laboratory Report LAUR 86-748, 2004.
[19] B.H. Toby, EXPGUI, a graphical user interface for GSAS, J. Appl. Crystallogr. 34 (2001) 210–221.
[20] C. Dong, PowderX: Windows-95 based program for powder X-ray diffraction data processing, J. Appl. Crystallogr. 32 (1999) 838.
[21] A. Boultif, D. Louer, Powder pattern indexing with the dichotomy method, J. Appl. Crystallogr. 37 (2004) 724–731.
[22] A. Le Bail, H. Duroy, J.L. Fourquet, Mater. Res. Bull. 23 (1988) 447–452.
[23] T. Hahn (Ed.), International Tables for Crystallography Volume A "Space-group Symmetry," Kluwer Academic Publishers, Dordrecht, 1992.
[24] A.V. Shubnikov, N.V. Belov, Colored Symmetry, Pergamon, Oxford, 1964.